Chinese Chemical Letters 34 (2023) 108076

Contents lists available at ScienceDirect

Chinese Chemical Letters

journal homepage: www.elsevier.com/locate/cclet

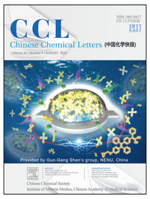

Cauliflower-like nanostructured ZnV_2S_4 as a potential cathode material to boost-up high capacity and durability of the aqueous zinc-ion battery

Mugilan Narayanasamy[a,b], Balakrishnan Balan[b], Chao Yan[a,*], Subramania Angaiah[b,*]

[a] School of Materials Science and Engineering, Jiangsu University of Science and Technology, Zhenjiang 212003, China
[b] Electro-Materials Research Laboratory, Centre for Nanoscience and Technology, Pondicherry University, Puducherry 605014, India

ARTICLE INFO

Article history:
Received 8 September 2022
Revised 27 October 2022
Accepted 14 December 2022
Available online 22 December 2022

Keywords:
Aqueous zinc-ion battery
Anion-exchange reaction
High-capacity cathode
Metal vanadium sulfides
Nano-ZnV_2S_4

ABSTRACT

Owing to their unique design and development, high safety and low-cost efficient cathode is still at the forefront of research for rechargeable zinc-ion batteries. However, the suitable cathode operating with ultrahigh capacity with a dendrite-free anode reaction mechanism remains challenging. In this, the first archetype of a high-rate and morphologically stabled cathode material is constructed from novel cauliflower-like nano-ZnV_2S_4 for aqueous zinc-ion batteries. Thus, nano-ZnV_2S_4 was prepared with an anion exchange reaction using $ZnV_2(OH)_8$ cauliflower-like nanostructured array as a template interestingly no morphological and shape changes were detected. The as-prepared nano-ZnV_2S_4 electrode reveals a specific discharge capacity of 348.2 mAh/g during 0.5 A/g with enhanced rate capability and excellent capacity retention of 89.2% at 4 A/g current density even after completing 1000 cycles.

In recent, due to the mounting exigency for developing green and sustainable energy storage for enormous applications, until now tremendous research efforts have been devoted to electrochemical devices such as flexible, portable electronic appliances and grid-scale long durable energy storage systems [1–5]. In this current alleviation of the global situation, it is not obligatory to shift completely to renewable energy sources and electric-powered vehicles [6]. Till date, the progress toward these energy storage technologies tends to utilize both renewable energy and electric vehicles with the high power density and fast recharge capability are still immature and require further development [7–9]. The majorly utilized substitutes for commercial usage of lithium and sodium-ion batteries (LIBs and SIBs) are still complicated since they have superior cycle performance and higher specific energy, which open up in a wide range of applications [10]. These major concerns over their safety, limited recycling infrastructure, restricted Li resources, and environmental impact are being deployed in real-life applications [11,12]. Comparatively, the water-based aqueous electrolytes endow rechargeable batteries with low cost and superior safety precautions. In this regard, the rechargeable aqueous zinc-ion battery offers a high-security and low-cost pathway on futuristic energy storage devices owing to the merits of decreased toxicity level and inimitable global abundance of earth sources of zinc [4,13,14]. However, these challenging roles remain constant in the manipulative preparation of cathodes since it has comparatively large radii of intercalated hydrated Zn^{2+} in robust electrostatic potency between its divalent Zn^{2+} and its host structures [3,15,16].

The diversity of V-O polyhedron structure leads to many types of V-based oxides. In addition, with the change in V valence state (V^y; $y = 2^+$, 3^+, 4^+, 5^+), the structure of the V-O polyhedron also changes simultaneously, resulting to an assortment of vanadium oxides with diverse compositions and structural skeletons [17]. During earlier investigations on vanadium materials for ZIBs are majorly fixated on vanadium oxides such as orthorhombic V_2O_5 [18], bilayered $V_2O_5\cdot nH_2O$ [19], $V_2O_5@V_2C$ [5], VO_2 [20], $V_2O_x@V_2CT_x$ [21], $K_{0.25}V_2O_5$ [22], $Na_6V_{10}O_{28}$ [23], Zn-V_2O_5 [24], $V_6O_{13}\cdot nH_2O$ [25], V_2O_3@AC [26] and $V_5O_{12}\cdot 6H_2O$ [27], endure its structure with repeated implantation of Zn^{2+} ions. Similarly, the rise of vanadium-based Transition Metal Dichalcogenides (TMDs) with diverse crystal structures and also rare distinctive physical and chemical properties exhibit better electrochemistry due to the vanadium's multi-valence state and large ion transfer channel [28–33]. They mainly attribute the electrochemical energy storage performance to diverged vanadium oxidation states with low

---

* Corresponding authors.
E-mail addresses: chaoyan@just.edu.cn (C. Yan), a.subramania@gmail.com (S. Angaiah).

https://doi.org/10.1016/j.cclet.2022.108076

operating voltage and because of their suitable open-framework structures [34–36]. Very recently, researchers showed attention more to bimetallic compounds as a newer cathode material because of their advantages besides mono-metallic compounds. In particular, the spinel structure binary metal oxides ($M_xV_mO_n$, M = metal cations) have been triggered more *via* investigating their electrochemistry it is found to be the most promising cathode materials with benefits such as widened potential window, more active sites, superior conductivity, and improved cycling stability. Recently, Liu *et al.* firstly demonstrates about this typical spinel ZnV_2O_4 by a significant electro activation process during the initial electrochemical sequences the occurrence of vanadium's mixed-valence state acts as a stochiometric conductive frame which enhances their stable high capacity and excellent cyclic stability for aqueous ZIBs [37]. Li *et al.* have reported porous like ZnV_2O_4 particles coated with N-doped carbon (ZnV_2O_4/C–N composite) synthesized *via* pyrolysis technique which showcases a specific discharge capacity of 301 mAh/g at 300 mA/g current density [38]. Furtherly, Tang *et al.* recommended that a new novel urchin-like magnesium vanadate could provide an enlarged specific surface area with induced more active sites, shortens the conduction channel of the host electrolyte ions, and affordable structural stability that helps for better electrochemical performance on aqueous zinc-ion batteries (AZIBs) [39]. Noticeably, it is observed that the binary metal vanadate has a drawback on structural degradation with the influence of reactant solvent in it further leading to low cycling stability [40]. From the recent research, it is evidenced that the development of interest in metal vanadium sulfides (MVS) as an electrode with more sophisticated electrical conductivity than all other oxide counterparts of it, because of much inferior optical bandgap in sulphides than oxides and more potentially viable in energy storage materials [41–43].

In concern to the above-mentioned issues, we developed a highly standardized novel cathode material by accomplishing a high rate and stable electrochemical performance for ZIBs. The innovative design of a bimetallic sulfide-based zinc-ion battery was fabricated by employing a cauliflower-like nano-ZnV_2S_4 as a cathode. It delivered an admirable specific discharge capacity (348.2 mAh/g during 0.5 A/g), and the interface engineering of the following MVS nanostructure contributes to good cyclic stability (~89.2% retention after 1000 cycles@4 A/g). This better electrochemical involvement of sulfide electrodes, when compared to other oxide electrodes, is mainly attributed to two major reasons such as truncated electronegativity and the enormous particle size of sulfur that builds tightly bonded structure and improved ion transfer assets.

Synthesis of ZnV_2S_4: In a distinctive synthesis process, 2 mmol of ammonium metavanadate (NH_4VO_3) was added into a mixture of 50 ml of ethylene glycol and 20 mL of deionized water. After a few minutes of sonication, 1 mmol/L of zinc nitrate ($Zn(NO_3)_2$) was added to the above solution and dynamically stirred until it attains a homogeneous solution. To this, 3 mmol/L of oxalic acid [$H_2C_2O_4$] was added as a chelating agent. Subsequently, 50 mL of 30% H_2O_2 and 70% HNO_3 were added dropwise into the mixture solution. This final solution mixture was then transferred and maintained at 180 °C for 12 h in 100 mL of Teflon-lined autoclave, and then chilled to room temperature to get a black-colored $ZnV_2(OH)_8$. The precipitates were collected and washed repeatedly with deionized water followed by absolute ethanol, finally dried in a vacuum furnace at moderate room temperature. Further, the initially prepared $ZnV_2(OH)_8$ sample and 0.1 mol Na_2S were diluted in 70 mL of DI water and engaged in an autoclave and heated at 120 °C for 8 h. In this process, $ZnV_2(OH)_8$ reacts with sulfide ions and replaces the OH^- functional group to form cauliflower-like nano-ZnV_2S_4. All the samples were repeatedly washed with de-ionized water and kept drying for 12 h at 80 °C for further usage.

The XRD analysis (Empyrean, Malvern Panalytical) from the range 5°–80° in the presence of nickel-filtered Cu-Kα ($\lambda = 1.54$ Å) radiation at an increment of 0.05° was utilized to examine the phase purity of the prepared material. The (Renishaw RM 2000) confocal micro-Raman spectrometer instrument was used to record its bandgap spectra by passing a 10 mW Ar^+ laser under 516 nm. X-ray photoelectron spectroscopy (XPS) (Model: PHI 5000 VersaProbe III) is favored to analyze the surface elements in monochromatized Al-Kα. The morphology of nano-ZnV_2S_4 was analyzed using FESEM (CARL ZEISS, Model: Sigma with Jemini column, USA). The morphology of nano-ZnV_2S_4 and its elemental compositions were confirmed by TEM (JEM-2010F) and energy-dispersive X-ray spectroscopy (EDAX), respectively.

To examine the electrochemical proficiency of the as-prepared ZnV_2S_4 sample, the coin-cell of CR2032 was built with ZnV_2S_4 as the cathode, Zn sheet (0.62 mm with purity phase > 99.99%, Alfa Aesar) as anode (where $E = -0.76$ V *vs.* SHE), Waterman filter paper as the separator and 2 mol/L $ZnSO_4$ of acidic phase was used as water-based electrolyte. The working electrode consists of ZnV_2S_4, acetylene black, and poly(tetrafluoroethylene) as the tightly bonded binder in *N*-methyl-2-pyrrolidone (NMP) with a standardized weight ratio of 70:20:10 to prepare a homogeneous slurry. This slurry paste was applied onto the graphite sheet and kept under a vacuum furnace for 12 h at 90 °C to decay the solvent present in it. After cooling, the slurry-coated film was made sliced into circular disks of 15 mm. The mass loading of each cathode disk is maintained under 0.8–1.4 mg/cm^2 with an approximate thickness of ~4 µm.

All the electrochemical assessments were carried out by using a Biologic electrochemical workstation (Model: VSP, (France)). The cyclic voltammetry curves were decoded in the fixated potential window of 0.3–1.7 V at numerous scan rates of 0.25, 0.5, 1, 2, 5 mV/s. GCD (Galvanostatic charge-discharge) curves were recorded at different current densities of 0.5, 1, 2, 4 and 8 A/g in the potential range of 0.3–1.7 V. the electrochemical impedance measurements were recorded in an average frequency range of 0.01 Hz–100 kHz in open circuit potential with 5 mV of AC amplitude.

Hydrothermal synthesis is a majorly utilized simple technique for the preparation of nanostructures by establishing unique morphologies. In this study, we employ binary-step hydrothermal synthesis for forming this novel cauliflower-like nano-ZnV_2S_4 by a self-assembly process [37,39,44–49]. Here, the formation mechanism of cauliflower-like nano-ZnV_2S_4 arrays from $ZnV_2(OH)_8$ nanoparticles can be explained based on ion-exchange reaction as illustrated in Fig. 1 [40]. The reaction mechanism for the preparation of cauliflower like nano-ZnV_2S_4 is mentioned below.

$$2NH_4VO_3 + 2C_2O_4H_2 + 2H_2O \rightarrow 2VO_2 + 2NH_4OH + 6H_2O + 2CO_2 \uparrow \quad (1)$$

$$2VO_2 + Zn(NO_3)_2 + 4H_2O \rightarrow ZnV_2(OH)_8 + 2NO_2 \uparrow \quad (2)$$

$$4Na_2S \rightarrow 8Na^+ + 4S^{2-} \uparrow \quad (3)$$

$$ZnV_2(OH)_8 + 8Na^+ + 4S^{2-} \rightarrow ZnV_2S_4 + 8NaOH \quad (4)$$

The growth mechanism of cauliflower-like nano-ZnV_2S_4 might be involved in a multistep reaction process. Primarily, from Eq. 1 during the initial step of the hydrothermal heat treatment at 180 °C, the NH_4VO_3 is reduced to $2VO_2$ through the inclusion of oxalic acid as a reducing agent. Meanwhile, during step two $Zn(NO_3)_2$ is readily decomposed to its preformed state as ZnO nanoclusters as per Eq. 2. These nanoclusters are then self-restacked into nanoparticles to shrink their surface tension on the dispersed nanoclusters to form a by-product $ZnV_2(OH)_8$ nanoparticles are generated from the intermediates $2VO_2$ and ZnO. During the final step of hydrothermal heat treatment, from Eqs. 3 and 4,

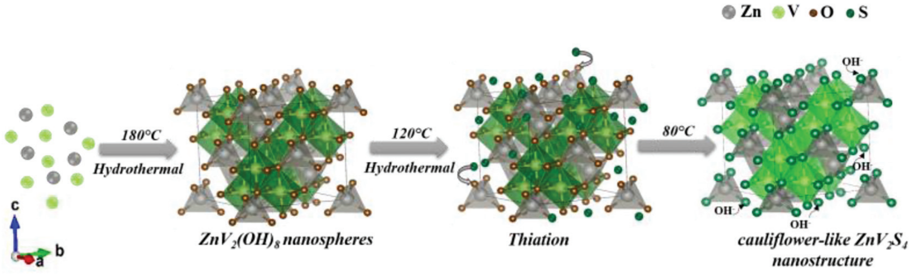

Fig. 1. Schematic illustration for the preparation of cauliflower-like nano-ZnV_2S_4.

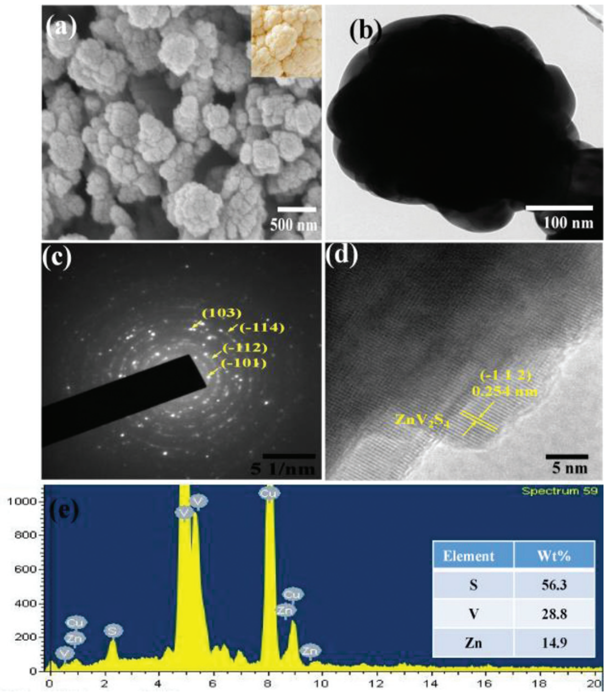

Element	Wt%
S	56.3
V	28.8
Zn	14.9

Fig. 2. (a) FE-SEM image of nano-ZnV_2S_4 (Inset shows cauliflower-like image). (b) TEM image of ZnV_2S_4. (c) SAED pattern of ZnV_2S_4. (d) HR-TEM images of ZnV_2S_4. (e) EDAX mapping image of ZnV_2S_4.

the $ZnV_2(OH)_8$ reacts with sodium sulfide at 120 °C and replaced the OH^- functional group with S^{2-} to form cauliflower-like nano-ZnV_2S_4.

The FE-SEM images (Fig. 2a) of nano-ZnV_2S_4 show that the metal nanoparticles tend to aggregate themselves and eventually form a randomly arranged disordered nanostructure, which is composed of agglomerates of pseudo-spherical nanoparticles. Such integrated nanoparticles formed from the self-assembly of many nanoparticles are decorated like unique cauliflower-like structures with an average size of ~300 nm. This empowers the penetration and helps in the ultrafast transportation of electrolyte ions during the reaction process. Further, The TEM image (Fig. 2b) confirms the interconnected network structure of cauliflower-like nano-ZnV_2S_4 by exhibiting a globular shaped morphology and good dispersity. The SAED pattern (Fig. 2c) shows a typical building block labelled by the white dotted line circles reveal with a lattice fringe *d*-spacing of 0.138, 0.254, 0.214 and 0.146 nm corresponding to the ($\bar{1}$01), ($\bar{1}$12), ($\bar{1}$14) and (103) planes, respectively. The HR-TEM profile of Fig. 2d discloses that lattice fringe of 0.254 nm is indexed to (−112) plane matched suitably to nano-ZnV_2S_4 with good crystallinity. The lattice fringe of the energy-dispersive spectrum analysis (Fig. 2e) demonstrates the presence of S, V and Zn along with the weight percentage of 56.6%, 28.8% and 14.9%, respectively, it is also additionally consistent in our following XRD and XPS findings.

The XRD technique is utilized to recognize its crystalline phase and the structural composition of cauliflower-like nano-ZnV_2S_4 as represented in Fig. 3a. The diffraction peaks which correspond to 2θ values of 17.43°, 34.86°, 44.6°, 52.03°, 63.52°, 66.02°, 72.8° and 75.10° are indexed and well-matched to the patters of ($\bar{1}$01), ($\bar{1}$12), ($\bar{1}$14), (103), (202), (008), (203) and (224) respectively. All the diffraction maxima could be indexed with the standard pattern of NiV_2S_4 (JCPDS No. 76–1058). In our case, Instead of Nickel peaks, the combination of ZnV_2S_4 is also well addressed by ZnS (JCPDS No. 79–2204). Further, it is asserted that the top layer of ZnV_2S_4 nanostructure contains some OH^-, while its bulk is made fully nano-ZnV_2S_4. Therefore, it is competent to provide high pure ZnV_2S_4, and maintaining the particular ratio of reactant and solvent plays a key role to obtain a highly pure form of nano-ZnV_2S_4. Thus, XRD results confirm the successful substitution of $ZnV_2(OH)_8$ into cauliflower-like ZnV_2S_4 nanostructures. The nano-ZnV_2S_4 is further characterized by Raman spectroscopy (Fig. 3b). the prominent peaks detected at 259.75 cm^{-1} and 379.4 cm^{-1} are corresponds to the in-plane E_{1g} and A_{1g} vibration modes which strongly belongs to VS_4, correspondingly [50]. the band wave located at 467.2 cm^{-1} can be attributed to the sulfur bond or their combination [51]. The Zn-S shows its characteristic phonon modes with high intensity at 797 cm^{-1}. the weak band waves of nano-ZnV_2S_4 located at 125.58 cm^{-1} (stretching and bending vibrations of V–S bonds), 865.18 cm^{-1} (V-S-V bond vibration), and 914 cm^{-1} (vibration of V=S bonds) [52].

The nano-ZnV_2S_4 valance states and their chemical structure are analyzed by XPS analysis (Fig. 4a). The full spectrum survey indicates that synthesized cauliflower-like nano-ZnV_2S_4 contains V, Zn and S. All the values of the peaks are perfectly associated with V 2p, Zn 2p and S 2p, respectively. Through peak deconvolution of the V 2p spectrum (Fig. 4b), the occurrence of vanadium during mixed valance state of V^{4+} and V^{3+} is confirmed, which is more beneficial for the Zn-ion storage mechanism [53]. The spin-orbit distance between $2p_{3/2}$ and $2p_{1/2}$ peaks for V^{4+} and V^{3+} is measured to be 513.42, 517.46, 520.96 and 524.71 eV, which correspond to the previously reported values [5,54]. Fig. 4c Meanwhile the S 2p core level spectrum characteristic of the sulfide S^{2-} ligand shows a doublet with S $2p_{2/3}$ and S $2p_{1/2}$ binding energy of 160.58 and 164.15 eV [41]. As shown in Fig. 4d, it is clear that zinc ions are present in the bivalent state with two distinctive peaks at 1021.49 and 1043.7 eV, respectively [55].

To understand the electrochemical behavior of nano-ZnV_2S_4 cathode material for zinc ion battery was examined in an aqueous 2 mol/L $ZnSO_4$ electrolyte solution. The fabricated CR2032 coin cell is initially tested using cyclic voltammetry (CV) at 2 mV/s of scan rate in the fixed potential range of 0.3–1.7 V *versus* Zn^{2+}/Zn. The resultant CV profile is substantially overlapped and highly reversible (Fig. 5a). It demonstrates the great reversibility of ZnV_2S_4. On both cathodic and anodic sweeps, two significant redox peaks are seen, corresponding to Zn^{2+} intercalation/de-intercalation of ZnV_2S_4. The cathodic/anodic sweep reflects the two pairs of redox couple at 0.823/0.49 and 1.17/0.75 V representing the V^{4+}/V^{3+} couple. This

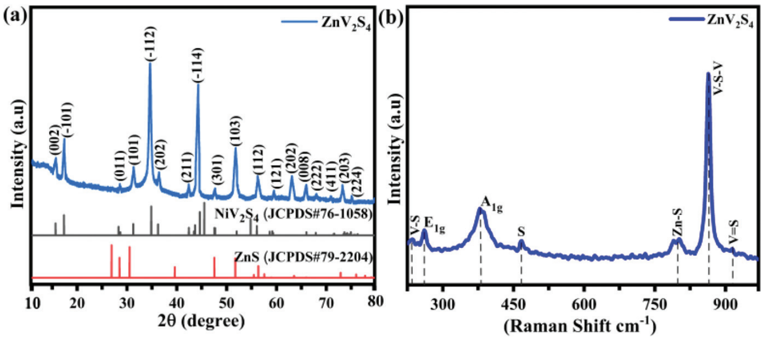

Fig. 3. (a) XRD pattern of nano-ZnV_2S_4. (b) Raman spectrum of nano-ZnV_2S_4.

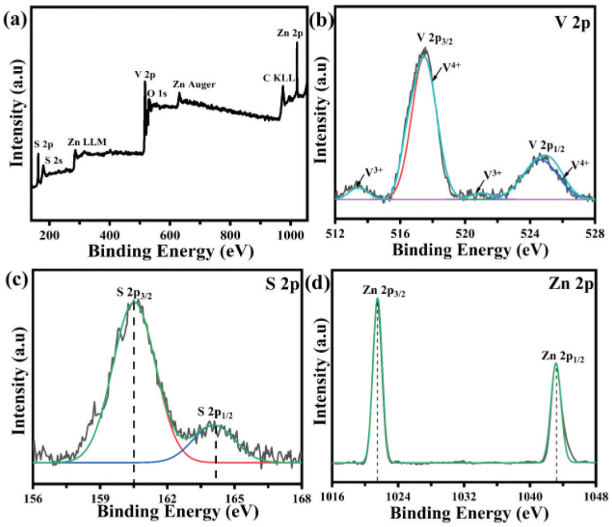

Fig. 4. (a) The full XPS spectrum of nano-ZnV_2S_4. (b–d) High-resolution XPS spectrum of V 2p, S 2p and Zn 2p.

vanadium multiphase redox couple often produces electrochemical performance in multistep intercalation/de-intercalation with different charge carriers for bimetallic vanadium-based oxides and sulfide materials [56]. The electrochemical reaction kinetics of ZnV_2S_4 cathode are explored at various scan rates ranging from 0.25 mV/s to 5 mV/s (Fig. 5b). It indicates that the CV curves increasingly widen the peaks and increased the peaks current while a raise in scan speeds further. This suggests the predominant contribution by diffusion reaction and a considerable capacitive contribution.

Fig. 5c implies that log(i) *vs.* log(ν) plot for nano-ZnV_2S_4. Thus, coordination between these peak currents (i) and the following sweep rate (ν) in the all-CV curve tested at various scan rates reflects the charge storage reaction of cauliflower-like ZnV_2S_4.

$$i = a\nu^b \tag{5}$$

$$\log(i) = \log(a) + b\log(\nu) \tag{6}$$

From Eqs. 5 and 6 [5], the intended b values of the corresponded peaks R1 and R2 were determined to be 0.89 and 0.92, respectively for discharge; and for the peaks O1 and O2, during charge, the b values are found to be 0.86 and 0.94, respectively. Thus, the ratio of capacitive and diffusion contribution of nano-ZnV_2S_4 at different sweep rates is shown in Fig. 5d. Surface-controlled capacitance progressively increases as the sweep rate increases, it designates that the electrode is more surface-controlled capacitance rather than diffusion-controlled capacitance. Further, it is also enduring the cauliflower-like ZnV_2S_4 to attain high-rate capability for the Zn^{2+} ion storage.

In elucidatory with the miscellaneous electrochemical behavior of ZIB, to evaluate the material's capability *via* half-cell configuration by using nano-ZnV_2S_4 as electrode material and a standardized anode as zinc plate. The galvanostatic charge/discharge profile comparison of Zn//ZnV_2S_4 at different current densities ranging from 0.5 A/g to 8 A/g is shown in Fig. 6a. Clear charge/discharge slopes and plateaus perfectly correspond to their redox mechanism on its subsequent CV curves, which is directly related to its unique morphology. The interconnecting dark spots inside each cauliflower-like nanostructured ZnV_2S_4 provide numerous spacer junctions that allow easy distribution of the electrolyte towards reducing the diffusion resistance of the electrolyte. Further, a prominent discharge specific capacity of 348.2 mAh/g during 0.5 A/g is attained due to their improved penetration of more Zn^{2+} ions into pores during the charging-discharging process.

In the charge/discharge process, the Zn^{2+} ions of the host electrolyte solution enclosures onto the cathode, and the Zn anode drops electrons to yield Zn^{2+} that diffuses back to the electrolyte to keep up the charge steadiness of the electrolyte. During its irreversible process, the movement of Zn^{2+} passes from the cathode towards the electrolyte, and the Zn^{2+} in the obtained electrolyte tends the electrons in friction to deposit on the Zn anode.

Furthermore, the cauliflower-like ZnV_2S_4-based AZIB upholds extreme durability of 70.6% specific capacity retention even after it is augmented till the 16-fold increase of its current density, it indicates a steady reaction with less ionic polarization due to their dominancy and interface engineering on the surface-based conveyance. The high remarkable rate capability is strongly attributed to the novel cauliflower-like structured ZnV_2S_4-based cathode material contributed to a better charge transfer rate and curtails the ion transfer pathway (Fig. 6b). It attains a linear specific discharge capacity of 348.2, 307.6, 284.71, 265.93 and 246.04 mAh/g at 0.5, 1, 2, 4 and 8 A/g, respectively. Overall, this superior rate capability of ZnV_2S_4 is compared with the previously reported bimetallic transition metal oxides/sulfides based AZIBs electrode (Table S1 in Supporting information).

The long-term cycling performance of the Zn//ZnV_2S_4 battery is explored and shown in Fig. 6c. When the cycling performance begins at their initial stage, the electrode seems to be fully activated and tends to linear specific capacity drop occurs from 265 mAh/g very slowly and maintains the electrode steady with accomplishing 89.2% capacity retention for 4 A/g high current density even after 1000 cycles. Fig. 7a represents the Zinc storage mechanism in the ZnV_2S_4 electrode. It is evident by the diminished resistivity and enhanced reaction kinetics of ZnV_2S_4 and finally, it can facilitate effectual electron transportation and more diffusion pathways for the Zn^{2+} storage mechanism. In addition, the energy density of this battery is 361.09 Wh/kg at a power density of 288.6 W/kg. Those power and energy densities are counted and compared across state-of-the-art power sources (Fig. 7b), in which one can see that the ZnV_2S_4-based ZIB system delivers superior

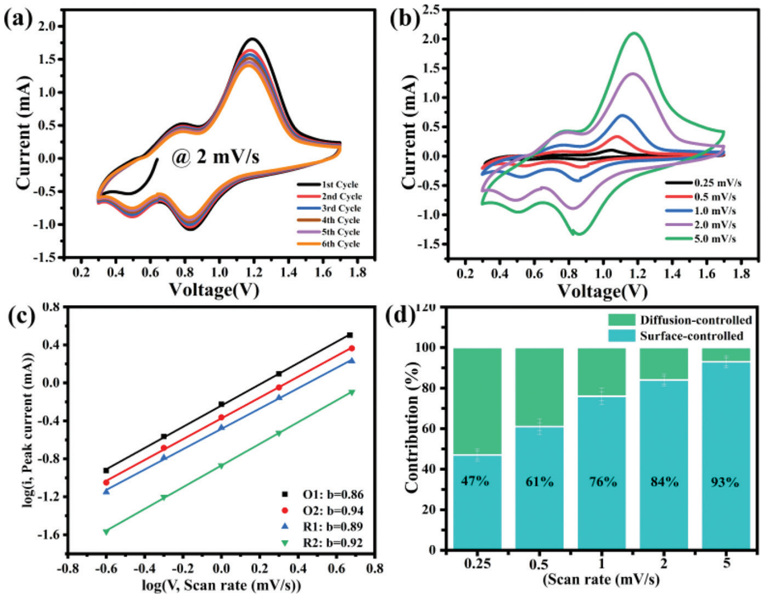

Fig. 5. (a) The CV curves of nano-ZnV_2S_4 at 2 mV/s during various cycles. (b) CV curves of nano-ZnV_2S_4 at different sweep rates. (c) log(i) *vs.* log(v) plot for specific peak current values. (d) Its equivalent capacitive contribution at various sweep rates.

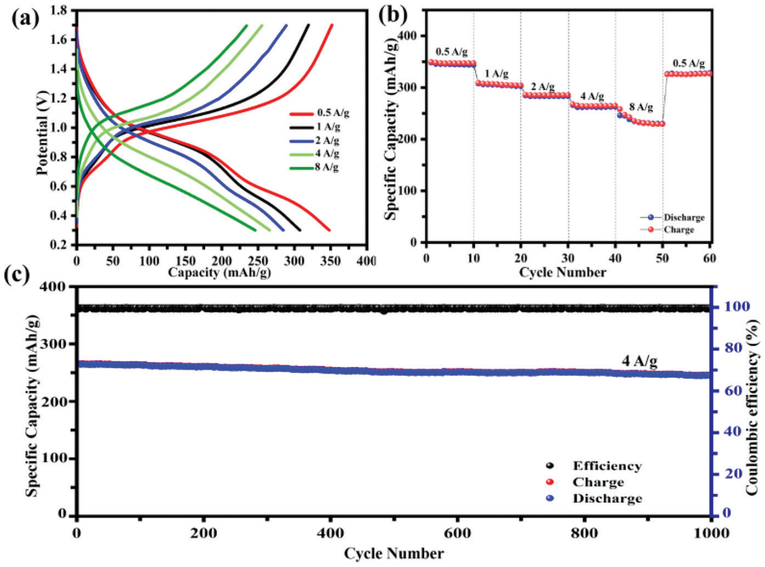

Fig. 6. (a) GCD curves of nano-ZnV_2S_4 electrode. (b) Rate performance of nano-ZnV_2S_4 electrode. (c) Long-term cycling performance of nano-ZnV_2S_4 electrode at 4 A/g.

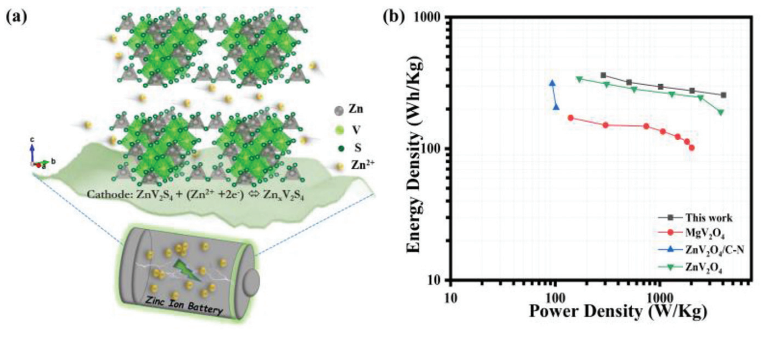

Fig. 7. (a) Schematic illustration of zinc storage mechanism in ZnV_2S_4 electrode. (b) Ragone plots of nano-ZnV_2S_4 electrode compared with previously reported cathodes for ZIBs.

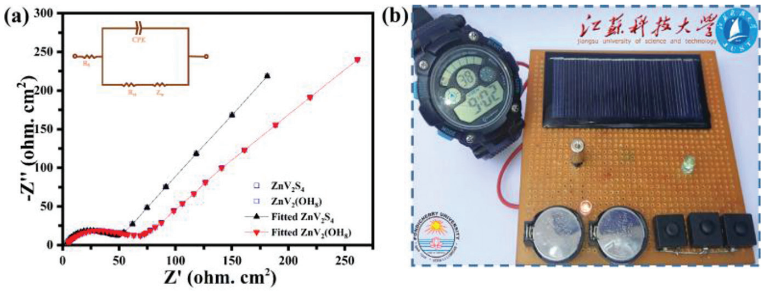

Fig. 8. (a) Nyquist plots of Zn//ZnV_2S_4 and Zn//$ZnV_2(OH)_8$ cells in 2 mol/L $ZnSO_4$ aqueous electrolyte and the inset shows an equivalent circuit for the Nyquist plots of nano-ZnV_2S_4 and nano-$ZnV_2(OH)_8$. (b) The real-time image shows the demonstration of Zn//ZnV_2S_4 based ZIB power supplied by a solar energy conservation system.

electrochemical performance [37–39]. Furtherly, fewer electronegative sulfur ions with more active bonds result in a strong adhesion between other metal ions. The larger size and polarizability of 3p orbital of sulfur is compared to 2p orbital of oxygen reduces the structural strain formed during ion insertion, because the stain developed in the bigger 3p orbital is lower, thereby causing better cycling stability [57]. Hence, the formation nature of scaffolding nanostructured framework is widely reported in several ion batteries and proved to be one of the essential methods in mitigating their volumetric energy changes during the charge/discharge cycle. These outcomes indicate a high retainability of nanostructure even after repeated long cycling stability as previously reported [58–64].

The electrochemical impedance spectra measurement (EIS) is accomplished to know further deeply to enhance the electrochemical performance of ZnV_2S_4 are projected in Fig. 8a. The Nyquist plots are likely similar to the well-compressed semicircle from the high-frequency range to the low-frequency range, a line tending at approximately 45° in the low-frequency range. The inset figure shows an equivalent circuit for the Nyquist plots of nano-ZnV_2S_4 and nano-$ZnV_2(OH)_8$, the compressed semicircle defines the charge transfer resistance (R_{ct}), and the inclined line is denoted as Warburg impedance (Z_W). In similar, R_s represent the ohmic resistance of the electrode, including the electrolyte and cell components. Where CPE and Z_w are the capacitance related to double layer and Warburg impedance, respectively [65]. Besides, a slope from the lower frequency range upsurges simultaneously shows enhanced ion diffusion kinetics. The electrode, ZnV_2S_4 shows the Rct value of 48.2 Ω with a significantly diminished charge-transfer resistance which is much lower than that of the $ZnV_2(OH)_8$ (63.7 Ω) electrode. Simultaneously, it indicates faster ion transfer during the electrode-electrolyte interaction. While the charge transfer resistance decreased, the kinetics of cauliflower-like nano-ZnV_2S_4 gets improved and thus empowers the penetration and fast conduct transport of electrolyte ions and support them for more diffusion pathways for zinc ions [66]. Fig. 8b shows an attempt to utilize the stored renewable solar energy in aqueous ZIBs has been prepared, from that the sustainable solar energy can be harvested for self-charging of the Zn//ZnV_2S_4 battery device, where the red lamp blinking indicates the charging process. In this, two aqueous ZIB devices are connected in series and can easily light a bright green lamp (3 W). Meanwhile, it also runs the commercial digital clock normally. The aqueous ZIB is an efficient alternative for commercially used sustainable energy storage devices that can look upon to practical energy demands making them more reliable in the portable/wearable electronic engineering field. Therefore, this work paves an innovative pathway for designing cauliflower-like nanostructured ZnV_2S_4 cathode material for aqueous ZIBs.

In conclusion, the cauliflower-like nanostructured ZnV_2S_4 spinel structure has been proven to store massive Zn^{2+} ions during the charging-discharging process and is reported as the first for aqueous ZIB. This Zn//ZnV_2S_4 cell exhibits a highly stable discharge capacity (348.2 mAh/g during 0.5 A/g), superior rate capability, and excellent long cycling stability (~89.2%) even after 1000 cycles@4 A/g. Additionally, a good structural framework is retained even after repeated implantation of Zn^{2+} which is attributed to the intact spinal structured ZnV_2S_4 and its stable form even after certain phase transformation. These results pave a new pathway for the preparation of low-valent bimetallic vanadium-based sulfide materials by a unique anion-exchange reaction mechanism with superior electrochemical performance for aqueous zinc-ion batteries.

Declaration of competing interest

The authors declare that they have no conflict of interest.

Acknowledgments

The authors acknowledge the funding for this project through the National Nature Science Foundations of China (No. 51873083), Jasmine Jiangsu Fellowship of Jiangsu Province (No. 180511800007), and the Postgraduate Research & Practice Innovation Program of Jiangsu Province (No. SJCX20_1453).

Supplementary materials

Supplementary material associated with this article can be found, in the online version, at doi:10.1016/j.cclet.2022.108076.

References

[1] Q. Zhang, X. Cheng, C. Wang, et al., Energy Environ. Sci. 14 (2020) 965–974.
[2] B. Dunn, H. Kamath, J.M. Tarascon, Science 334 (2011) 928–935.
[3] M. Song, H. Tan, D. Chao, et al., Adv. Funct. Mater. 28 (2018) 1–27.
[4] J. Shin, J. Lee, Y. Park, et al., Chem. Sci. 11 (2020) 2028–2044.
[5] M. Narayanasamy, B. Kirubasankar, M. Shi, et al., Chem. Commun. 56 (2020) 6412–6415.
[6] S. Zuo, X. Xu, S. Ji, et al., Chem. Eur. J. 27 (2021) 830–860.
[7] M. Zhang, R. Liang, T. Or, et al., Small Struct. 2 (2021) 2000064.
[8] P. Yu, Y. Zeng, H. Zhang, et al., Small 15 (2019) 1–27.
[9] Y. Bai, Y. Hai, L. Cui, et al., Energy Technol. 11 (2021) 202000701.
[10] D.K. Maurya, B. Balan, V. Murugadoss, et al., Mater. Today Commun. 25 (2020) 101497.
[11] J. Ming, J. Guo, C. Xia, et al., Mater. Sci. Eng. R 135 (2019) 58–84.
[12] D. Selvakumaran, A. Pan, J. Mater. Chem. A (2019) 18209–18236.
[13] C. Xie, Y. Li, Q. Wang, et al., Carbon Energy 2 (2020) 540–560.
[14] B. Tang, J. Zhou, G. Fang, et al., J. Mater. Chem. A 7 (2019) 940–945.
[15] J. Li, N. Luo, F. Wan, et al., Nanoscale 12 (2020) 20638–20648.
[16] Z. Wu, Y. Wang, L. Zhang, et al., ACS Appl. Energy Mater. 3 (2020) 3919–3927.
[17] T. Zhou, L. Zhu, L. Xie, et al., J. Colloid Interface Sci. 605 (2022) 828–850.
[18] J. Zhou, L. Shan, Z. Wu, et al., Chem. Commun. 54 (2018) 4457–4460.
[19] T. Wu, K. Zhu, C. Qin, et al., J. Mater. Chem. A 7 (2019) 5612–5620.
[20] Y. Liu, P. Hu, H. Liu, et al., Mater. Today Energy 17 (2020) 1–7.
[21] R. Venkatkarthick, N. Rodthongkum, X. Zhang, et al., ACS Appl. Energy Mater. 3 (2020) 4677–4689.
[22] S. Li, M. Chen, G. Fang, et al., J. Alloy. Compd. 801 (2019) 82–89.
[23] T. Zhou, L. Xie, Q. Han, et al., Chem. Eng. J. 445 (2022) 136789.
[24] N. Zhang, Y. Dong, M. Jia, et al., ACS Energy Lett. 3 (2018) 1366–1372.
[25] J. Lai, H. Zhu, X. Zhu, et al., ACS Appl. Energy Mater. 2 (2019) 1988–1996.
[26] H. Chen, Y. Rong, Z. Yang, et al., Ind. Eng. Chem. Res. (2021) 2–10.

[27] N. Zhang, M. Jia, Y. Dong, et al., Adv. Funct. Mater. 29 (2019) 1–9.
[28] P. He, M. Yan, G. Zhang, et al., Adv. Energy Mater. 7 (2017) 1–5.
[29] H. Qin, Z. Yang, L. Chen, et al., J. Mater. Chem. A 6 (2018) 23757–23765.
[30] X. Pu, T. Song, L. Tang, et al., J. Power Sources 437 (2019) 226917.
[31] T. Jiao, Q. Yang, S. Wu, Z. Wang, et al., J. Mater. Chem. A 7 (2019) 16330–16338.
[32] L. Wang, Z. Wu, M. Jiang, et al., J. Mater. Chem. A 8 (2020) 9313–9321.
[33] Z. Wu, C. Lu, Y. Wang, et al., Small 16 (2020) 2000698.
[34] F. Xu, Y. Zhou, X. Zhai, et al., Small Methods 6 (2022) 2101212.
[35] J. Wang, C.F. Du, Y. Xue, et al., Exploration 1 (2021) 20210024.
[36] Y. Lu, H. Zhang, H. Liu, et al., Nano Lett. 21 (2021) 9651–9660.
[37] Y. Liu, C. Li, J. Xu, et al., Nano Energy 67 (2020) 104211.
[38] S. Li, L. Qin, L. Li, et al., Mater. Today Commun. 27 (2021) 102271.
[39] W. Tang, B. Lan, C. Tang, et al., ACS Sustain. Chem. Eng. 8 (2020) 3681–3688.
[40] R. Kumar, P. Rai, A. Sharma, J. Mater. Chem. A 4 (2016) 17512–17520.
[41] Y. Von Lim, S. Huang, Q. Wu, et al., Adv. Funct. Mater. 30 (2020) 1–10.
[42] Y. Zhang, T. Li, S. Cao, W. Luo, F. Xu, Chem. Eng. J. 387 (2020) 124125.
[43] L.T. Le, D.Q. Truong, T.T.D. Ung, et al., ChemistrySelect 5 (2020) 280–283.
[44] M. Shi, M. Narayanasamy, C. Yang, et al., Electrochim. Acta 334 (2020) 135546.
[45] M. Shi, B. Wang, C. Chen, et al., J. Mater. Chem. A 8 (2020) 24635–24644.
[46] Y. Liu, M. Shi, M. Han, et al., Chem. Eng. J. 387 (2020) 124104.
[47] M. Shi, P. Xiao, J. Lang, C. Yan, X. Yan, Adv. Sci. 7 (2020) 1901975.
[48] C. Xia, J. Guo, P. Li, et al., Angew. Chem. Int. Ed. 57 (2018) 3943–3948.
[49] P. He, Y. Quan, X. Xu, et al., Small 13 (2017) 1–7.
[50] T. Chen, X. Zhu, X. Chen, et al., J. Power Sources. 477 (2020) 228652.
[51] J. Liu, W. Peng, J. Mater. Chem. C 9 (2021) 6308–6315.
[52] J. Ding, H. Gao, W. Liu, et al., J. Mater. Chem. A 9 (2021) 11433–11441.
[53] M. Narayanasamy, L. Hu, B. Kirubasankar, et al., J. Alloy. Compd. 882 (2021) 160704.
[54] M.C. Biesinger, L.W.M. Lau, A.R. Gerson, et al., Appl. Surf. Sci. 257 (2010) 887–898.
[55] Y.C. Liang, C.C. Wang, RSC Adv. 8 (2018) 5063–5070.
[56] P. Byeon, Y. Hong, H.B. Bae, et al., Nat. Commun. 12 (2021) 1–11.
[57] J.B. Goodenough, Solid State Ion. 69 (1994) 184–198.
[58] L. Xiao, Y. Zhao, J. Yin, L. Zhang, Chem. Eur. J. 15 (2009) 9442–9450.
[59] F.K. Butt, M. Tahir, C. Cao, et al., ACS Appl. Mater. Interfaces 6 (2014) 13635–13641.
[60] Y. Jin, J. Xu, L. Wang, et al., Chem. Eur. J. 22 (2016) 18859–18864.
[61] Q. Pan, X. Yang, X. Yang, et al., RSC Adv. 8 (2018) 17754–17763.
[62] L. Yang, M. Huang, M. Lu, et al., Chem. Eng. J. 364 (2019) 462–474.
[63] H. Xuan, H. Li, J. Gao, et al., Appl. Surf. Sci. 513 (2020) 145893.
[64] Z. Shi, Q. Ru, S. Cheng, et al., Energy Technol. 8 (2020) 2000010.
[65] W. Xu, K. Zhao, Y. Wang, Energy Storage Mater. 15 (2018) 374–379.
[66] Y. Shi, B. Guo, S.A. Corr, et al., Nano Lett. 9 (2009) 4215–4220.